Establishment of an easy-to-construct liver injury mouse model for longitudinal analysis by drinking-water administration of MDA

Takumi Iwasaka[1, *], Tadahaya Mizuno[2, *, †], Katsuhisa Morita[1], Iori Azuma[1], Tomoka Nakagawa[1], Eri Nakashima[1], Hiroyuki Kusuhara[1]

[1]Graduate School of Pharmaceutical Sciences, the University of Tokyo, Bunkyo-ku, Tokyo, 113-0033, Japan
[2]Graduate School of Pharmaceutical Sciences, the University of Tokyo, Bunkyo-ku, Tokyo, 113-0033, Japan, Electronic address: tadahaya@gmail.com
†Corresponding author: Tadahaya Mizuno
*These authors contributed equally.

Author Contributions
TI: Data curation, Formal analysis, Investigation, Writing – Original draft, Visualization.
TM: Conceptualization, Resources, Supervision, Project administration, Writing – Original draft, Writing – Review and editing, Funding acquisition.
KM: Investigation, Data curation
IA: Investigation, Data curation
TN: Investigation
EN: Investigation
HK: Writing – Review and editing.

Address for Correspondence
tadahaya@gmail.com; Graduate School of Pharmaceutical Sciences, the University of Tokyo, Bunkyo-ku, Tokyo, 113-0033, Japan; Tel: +81-3-5841-4771

Financial support and sponsorship
This work was supported by the JSPS KAKENHI Grant-in-Aid for Scientific Research (C) (grant number 21K06663) and PAGS (grant number JP22H04925) from the Japan Society for the Promotion of Science, Takeda Science Foundation, and Mochida Memorial Foundation for Medical and Pharmaceutical Research.

Conflicts of interest
The authors declare that they have no conflicts of interest.

Abstract

Compound actions are diverse, capable of inducing various biological responses, making them a valuable exploratory tool for understanding biological mechanisms. While widely employed in liver dysfunction research, models requiring continuous administration for longitudinal studies come with high construction costs. Although drinking water models are useful, currently utilized compounds are limited, with thioacetamide being one of the few examples. Is it possible to expand drinking water models for liver dysfunction research? Addressing this question, our study focused on constructing a novel drinking water-induced liver injury model. Through data mining and literature research, 4,4'-methylenedianiline (MDA) was identified, whose drinking water administration consistently exhibited elevated ALT levels over 28 days. To evaluate differences in pathophysiological profiles compared to existing thioacetamide models, we acquired multi-view data of early biochemical test values, immune cell trafficking, and transcriptome over time. The analysis revealed unique features such as elevated total bilirubin in serum, increased monocyte-derived macrophages in the liver, and enhanced fibrinolysis in the liver, suggesting a model of cholestatic liver injury. This study proposes the first cholestatic liver injury model for compound drinking water administration, expanding the scope of longitudinal analysis in liver dysfunction research.

Introduction

Hepatic dysfunction, a condition with severe implications such as liver cancer and failure, has diverse causes, including drugs, alcohol, and hepatitis viruses (1,2). Despite its substantial public health impact, treatment options are limited, and there is a lack of medicine-based therapeutic approaches. Owing to its diverse nature, compound administration serves as a valuable tool for assessing biological responses, thereby enhancing our comprehension of disease pathophysiology (3). In hepatic dysfunction research, models induced by compounds like carbon tetrachloride (CCl_4) are widely employed, capable of inducing both liver injury and fibrosis (4–11). However, for longitudinal analysis emphasizing temporal changes, continuous administration during model construction can be a significant burden in the experimental process.

The model that involves continuous administration of compounds through drinking water is cost-effective and thus appealing to longitudinal analysis. Currently, the widely used drinking water-induced liver injury model is limited, predominantly involving thioacetamide (TAA) (12,13). Expanding and comparing drinking water-induced liver injury models beyond the TAA model is expected to facilitate a comprehensive analysis, combining the advantages of compound administration-induced injury models and those induced by drinking water, regarding both longitudinal and cross-sectional analyses. Then, is it feasible to expand the drinking water-induced liver injury model?

Here, this study pursued the establishment and evaluation of a drinking water-induced liver injury model using compounds other than TAA. Data mining and literature survey identified 4,4'-methylenedianiline (MDA) as a candidate hepatic toxicant not characterized in a drinking water-induced model (14,15). MDA administration via drinking water resulted in consistently elevated ALT levels over 28 days. Comparative analysis with the well-established TAA model revealed various differences in pathological profiles, assessed multi-view data composed of biochemical values, immune cell trafficking, and transcriptome profiles in the early administration phase. This research proposes an easily constructed, novel pathological profile for a drinking water-induced cholestatic liver injury model, with the potential to broaden the scope of longitudinal analyses in liver dysfunction research.

Materials and methods

Screening of candidate compounds for drinking water-induced liver injury model

Through database searches (CEBS, Open TG-GATEs, and DrugMatrix), compounds with ALT levels surpassing 200 U/L were extracted through administration regardless of route and time (16–18). Refined selection criteria with literature survey included: (a) the ability to induce liver dysfunction via oral administration, (b) water solubility (Solubility 1.0 g/L or greater), (c) cost-effectiveness, and ease of handling, and (d) a toxicity profile distinct from TAA, an existing drinking water-induced liver injury model.

Preparation of drug-induced liver injury models

Six-week-old male C57BL/6JJcl mice were purchased from CLEA Japan (Tokyo, Japan) and acclimatized for three to five days. The mice were exposed to Thioacetamide (T0817, Tokyo Chemical Industry Co., Japan) or Methylene dianiline (M0220, Tokyo Chemical Industry Co., Japan) dissolved in drinking water (300 mg/l or 750 mg/l) to induce liver damage, whereas the controls received a tap water. Mice were sacrificed at each time point and perfused liver samples and blood were harvested (Liver and blood sample collection section). The procedures reported in this article were performed in accordance with the guidelines provided by the Institutional Animal Care Committee (Graduate School of Pharmaceutical Sciences, the University of Tokyo, Tokyo, Japan).

Liver and blood sample collection

In the early phase (1, 2, 3, 4, and 8 day), the blood was collected through an inferior vena cava into 1.5 mL tube containing 1 μL heparin (Yoshindo Inc, Toyama, Japan) and a superior vena cava was clipped using a clamp. After cutting the portal vein, the first perfusion was performed by injecting 10 mL of 5 mM HEPES (H4034, Sigma-Aldrich Co. LLCUSA) / 5 mM EDTA (345-01865, Fujifilm Corporation) Hanks' Balanced Salt Solution (17461-05, Nacalai Tesque, INC., Japan) through the inferior vena cava. Then, the second perfusion was performed by using 10 mL of 5 mM HEPES Hanks' Balanced Salt Solution. Before harvesting the tissue, 2 mL of dissociation enzyme solution of gentleMACS (Miltenyi Biotec, Germany) was filled in the liver from an inferior vena cava with clipping the cut portal vein. In the chronic phase (7, 14 and 28 day), the same process is performed up to the point before perfusion, the perfusion was performed by injecting 20 mL of phosphate-buffered saline (PBS) through the inferior vena cava. For the obtained liver, a portion of the outer left latera lobe of the liver was subjected to RNA isolation (RNA-seq or qPCR analysis section) and the remaining tissue to flow cytometry analysis (Flow cytometry analysis section, acute phase only) or to the hematoxylin and eosin (H&E) stain (Histopathology section) or to western blotting, respectively. When observing the temporal changes in the blood biochemical values of the same individual, blood samples were collected from the tail vein. Details about data analysis are available in Supplementary information.

Analysis of blood specimens

The collected blood sample was centrifuged (1,700 g, 4 °C for 15 min) for serum separation. Serum alanine aminotransferase (ALT) and aspartate aminotransferase (AST) were measured using a DRI-CHEM NX500sV (Fujifilm Corporation, Japan). If the upper limit is exceeded, dilute with 100 mM HEPES with 0.1% CHAPS (pH 7.4, r.t.) and re-measured.

Analysis of liver specimens

Detailed procedures of RNA-seq analysis, Histopathology and flow cytometry analysis, including subsequent data analysis, are provided in Supplementary Information.

Quantitative PCR analysis

Total RNA was prepared using ISOGEN II (311-07361, Nippon Gene Co., Ltd., Tokyo, Japan). RNA was reverse transcribed into cDNA using ReverTra Ace (TOYOBO, FSQ-301). Real-time PCR was performed using the THUNDERBIRD® Next SYBR® qPCR Mix (TOYOBO, QPX-201). Target gene expression was normalized to housekeeping genes Gapdh. Primers are listed in Table S1.

Clustering Analysis

Dimensionality reduction was performed using transcriptome of the liver at 1, 2, 3, 4, and 8 days after administration as features. All features were reduced in dimensionality by principal component analysis, multidimensional scaling, t distributed stochastic neighbor embedding, uniform manifold approximation and projection, spectral embedding and locally linear embedding. The dimensionally reduced features were combined using a meta-visualization method (19). The combined meta-distance matrix was visualized with a scatter plot, with each point color-coded by time and dose condition or ALT value. Note that transcriptome features were log-transformed. The detailed code used is found on GitHub (https://github.com/mizuno-group/MDAdrinkingwater). Analysis was performed using Python (version 3.10.6) with open-source packages (numpy, version 1.24.4; pandas, version 2.0.3; scipy, version 1.11.1; scikit-learn, version 1.1.2; statsmodels, version 0.13.2; umap, version 0.5.4)

Gene Set Analysis

First, the Gene Ontology (GO) annotation file (m5.go.v2023.1.Mm.symbols.gmt) was downloaded from

the MSigDB website (https://www.gsea-msigdb.org/gsea/msigdb) and used for the following analysis (20). In this part, the genes included in this GO annotation file were the genes to be analyzed. The transcriptome data were log-transformed, and genes with less than 70% (50 individuals) confirmed to be expressed were deleted. Subsequently, if the individuals with zero expression was biased toward a particular group by analysis of variance (one way repeated measures ANOVA), that genes was retained. Finally, missing values were complemented using KNNImputer (sklearn, version 1.1.2). The preprocessed RNA-seq data were subjected to Generally Applicable Gene-set Enrichment (GAGE) with following the GAGE algorithms comparing the control and the treated group for each model (21). After adapting GAGE, we obtained lists of GO terms with the mean difference and associated p value for each model and time point. To summarize and prioritize GO terms, we computed rank product statistics utilizing the mean difference values extracted from samples obtained at 48 and 72 hours, aligning with the respective ALT peaks for each model (22).

Results

Establishment of a drinking water-induced liver injury model using MDA

To establish a novel drinking water-induced liver injury model, we initially screened compounds inducing liver damage from large toxicology databases (16–18). Refined selection criteria were then applied, incorporating literature survey as in Methods section. From seven compounds meeting these criteria (Fluconazole, 4,4'-methylene dianiline, Suloctidil, Loratadine, N,N-dimethylformamide, Nitrosodiethylamine, Colchicine), 4,4'-methylene dianiline (MDA) stood out due to extensive studies as a liver carcinogen since 1970s, with reported drinking water administration tests for its carcinogenic evaluation (15,23). Despite reported oral administration-induced liver damage, the evaluation of MDA as a drinking water-induced liver injury model remains unexplored.

Therefore, MDA was administered via drinking water as a candidate compound. Biochemical tests at 7, 14, and 28 days from the start of administration revealed elevated levels of ALT, a marker of liver dysfunction, in both the MDA-treated and the existing TAA-treated groups (Fig. 1a, Table S2). Compared to the TAA-treated group, the MDA-treated group showed consistently higher ALT levels at day 7, and at day 14, the ALT values were significantly higher than those in the TAA-treated group. Subsequently, we evaluated liver fibrosis, a characteristic pathology of chronic liver dysfunction, using quantitative PCR. The results showed that, unlike the TAA-treated group, the MDA-treated group exhibited an increase in liver fibrosis markers such as Col1a1 and Acta2 at day 14 (Fig. 1b). This suggests that MDA administration via drinking water, similar to TAA, is a viable method for inducing a liver injury model. Hereafter, we refer to the liver injury models induced by drinking water administration of MDA and TAA

as the MDA-DW model and TAA-DW model, respectively.

Histological staining with H&E was performed on the liver collected during the administration trial, and the pathological images of the liver were observed. On the 7th day of administration in the TAA-DW group, a red region was observed, while in the MDA-DW group, a pale purple region was observed (Figure 1c). The region observed in the MDA-DW group is considered to be necrotic. Despite showing different pathological images, both models differed from the control group, confirming impairment of liver tissue. After observation, images were supplied to an anomaly detection model for extraction of the impaired regions and unbiased evaluation of their differences. Anomalous regions increased in both the TAA and MDA groups compared to the control group, with a particularly notable increase in the MDA group on days 14 and 28 (Fig 2a). Furthermore, principal component analysis using PCA was conducted on the feature vectors of each patch, resulting in roughly three groups: TAA-specific anomalous patch group, MDA-specific anomalous patch group, and a group containing both normal and anomalous patches (Fig 2b). Upon inspection of each patch, TAA-specific regions appeared as red areas, while MDA-specific regions exhibited small or absent nuclei against a pale pink background (Fig 2c, d). Thus, utilizing the anomaly detection model enabled unbiased confirmation of differing pathological anomalous regions between the TAA and MDA models.

Experimental Design for Comparing the Pathological Development Processes of MDA-DW Model and TAA-DW Model

As shown in Figure 1, both MDA-DW and TAA-DW models exhibit liver injury, but there are differences in the trend of biochemical markers and fibrosis markers. Do they present distinct pathological profiles as liver injury models? To assess the differences, we compared the temporal changes in the early phase of administration regarding pathological development from the following three perspectives (Figure 2):

1. Biochemical markers capturing macroscopic responses at the individual level.
2. Immune cell trafficking capturing the relationship between the liver and the immune system.
3. Transcriptome capturing molecular-level responses in the liver.

We obtained this multi-view data as shown in Figure 2.

Comparison of biochemical test results between MDA-DW and TAA-DW models

We compared biochemical test results capturing macro-level responses in both models. In the early stages of administration, the MDA-DW model exhibited a significant increase in liver dysfunction markers, including ALT, with a more gradual rise compared to the TAA-DW model (Fig. 3a, Table S3). The peak ALT value in the MDA-DW model occurred three days post-administration, contrasting with the TAA-DW model's peak at two days. Interestingly, both models showed substantial ALT recovery after the peak despite continued administration. Notably, the MDA-DW model displayed a pronounced increase in total bilirubin and total cholesterol compared to the TAA-DW model (Fig. 3b, c), suggesting a cholestatic-like liver dysfunction. This aligns with known MDA-induced cholestatic effects in single-dose oral administration studies (14). Consequently, the MDA-DW and TAA-DW models manifest distinct biochemical profile patterns.

Comparison of immune cell trafficking in MDA-DW and TAA-DW Models

Immune cell trafficking emerges as a pivotal factor in the progression of hepatic dysfunction (24–28). This study compares the immune cell trafficking capturing the interplay between the liver and the immune system in both models. Flow cytometric analysis (Fig. 4a, Fig. S4) unveiled a pronounced decline in lymphocyte population concurrent with elevated ALT levels, and a conspicuous augmentation in neutrophil population correlated with ALT elevation, observed consistently across both models. The values of neutrophils at the ALT peak exhibited substantial variability, strongly correlating with the degree of hepatic dysfunction, i.e., ALT levels (R=0.80) (Fig. 4b). Furthermore, Kupffer cells gradually diminished post-administration, accompanied by a compensatory rise in monocyte-derived macrophages. These results align with previous findings that monocyte-derived macrophages infiltrate the liver and differentiate in response to tissue injury (29). Notably, in the TAA-DW model, eosinophil accumulation was observed three and four days post-administration, a phenomenon absent in the MDA-DW model. In summary, immune cell trafficking in MDA-DW and TAA-DW models reveals shared behaviors among cell types indicative of liver injury models, yet it also highlights substantial differences in the behavior of certain cell types.

Comparison of transcriptome profiles in MDA-DW and TAA-DW models

Transcriptome profiles capturing the molecular responses of the liver were compared in both models. Employing META visualization (19), an integration of various dimensionality reduction methods was performed on individual gene expression data and visualized (Fig. 5). Results of each dimensionality reduction method used in META visualization are presented in Figure S2. When color-coded based on administered compounds and time, individuals shortly after administration in both TAA-DW and MDA-DW models initially positioned near the control group but diverged over time. Distinct clustering differences between the MDA-DW and TAA-DW models became evident with time progression (Fig. 5a). Conversely, among individuals sampled on day 8, the time point furthest from administration in this experiment, some were located close to the control group. Additionally, when visualized alongside ALT values, individuals with lower ALT values, regardless of the model, were positioned near the control group (Fig. 5b). Thus, both TAA-DW and MDA-DW models exhibited significant changes in expression profiles over time, with distinct temporal variations observed between the two models.

Analysis of distinct molecular mechanisms in MDA-DW model

Evaluation of macroscopic changes in the transcriptome profile revealed distinct molecular pathologies between the MDA-DW and TAA-DW models during the early stages of administration. To identify specific molecular mechanisms defining the pathophysiology of MDA-DW, Gene Set Analysis (GSA) was conducted. Transcriptome data obtained were subjected to Generally Applicable Gene-set Enrichment (GAGE) (Luo et al., BMC Bioinformatics, 2009), allowing application to gene expression datasets with varying sample sizes and experimental designs. Results indicated the presence of IL17 and monocyte-related Gene Ontology (GO) terms during the acute phase (48 and 72 hours) in the MDA-DW

model (Table S4). Visualization confirmed a similar trend in the TAA-DW model, suggesting common mechanisms underlying liver injury due to oral administration (Fig. 6a, Table S5). Conversely, fibrinolysis-related GO terms observed in the MDA model showed concentration in opposite directions between the TAA- and MDA-DW models (Fig. 6b, Table S4, S5).

Discussion

Compounds, owing to their diverse actions, can impart various perturbations to the biological system, serving as valuable exploratory tools for elucidating biological mechanisms (30–32). However, continuous administration of a compound poses high barriers, such as laborious costs for administration and elevated economic costs when mixed with diet. Limited options for longitudinal analysis include the labor-intensive historically established repeated-dose carbon tetrachloride model and the TAA drinking water model. This study proposes the MDA-DW model as a novel liver injury model conducive to easily constructed longitudinal analyses, with the potential to broaden the scope of longitudinal analyses in liver dysfunction research. To the best of our knowledge, this is the first cholestatic liver injury model via drinking water administration. The proposed model exhibits distinct pathophysiological profiles from the existing TAA-DW model, particularly highlighting intriguing differences in immune cell trafficking, a crucial factor in the progression of liver dysfunction. Noteworthy distinctions include the accumulation of eosinophils and the accumulation of monocyte-derived macrophages, observed exclusively in the TAA and MDA models, respectively (Fig. 4). In addressing the question of whether to expand the drinking water-induced liver injury model, this study focused on the MDA, which has a proven track record in drinking water administration studies. However, alternative candidate compounds were also found as described in the Result section. Thus, expanding liver injury models via drinking water administration of compounds is anticipated to enable future comprehensive analyses, contributing to a better understanding of the pathophysiological progression of liver dysfunction.

Model stability is essential for test reproducibility and delicate analyses. While the TAA-DW model is widely used as a model for drinking water-induced liver injury, instances of high mortality have been reported (33). The TAA-DW model in this study exhibits elevated ALT levels exceeding 10,000 U/l in the early stages, indicative of severe acute liver injury (Fig. 3). In contrast, the MDA-DW model shows milder liver dysfunction in the early stages, with ALT levels around 3,000 U/l, significantly less than the TAA-DW model. Notably, in continuous administration trials of the MDA-DW model, no fatalities have been observed so far. This proposed model could be a stable model with high individual survival rates.

Hepatic fibrosis is a crucial pathology in chronic liver dysfunction. Can the MDA-DW model be utilized for evaluating hepatic fibrosis? The MDA-DW model shows an elevation in fibrotic markers, including Acta2, at 14 days, followed by a decrease at 28 days (Fig. 1). In comparison, the TAA-DW model generally exhibits symptoms of hepatic fibrosis around 16-18 weeks (34). The distinctive temporal changes in hepatic fibrosis markers would be attributed to the activation of myofibroblasts derived from portal fibroblasts (PFs). Myofibroblasts, serving as a source of excessive extracellular matrix and playing

a significant role in hepatic fibrosis, are not present in normal liver tissue and are primarily activated by hepatic stellate cells (HSCs) or PFs (35). Iwaisako's study reports differences in the origin of myofibroblasts between the bile duct ligation (BDL) model, resembling cholestatic liver dysfunction, and the CCl_4 model, representing general liver dysfunction (36). In the CCl_4 model, over 80% of fibrotic cells originate from HSCs, maintaining a constant proportion regardless of time. In contrast, in the BDL model, over 70% of fibrotic cells originate from PFs, with the proportion decreasing over time. Considering the similar temporal changes between these models and the MDA-DW model's presentation of cholestatic liver dysfunction, as depicted in Figure 1b, it is inferred that PFs are primarily activated in the MDA-DW model. Further detailed assessments through long-term administration trials are necessary to determine its suitability for hepatic fibrosis pathology evaluation. However, as a model involving PFs' activation in liver dysfunction, the MDA-DW model, being convenient and stable without requiring surgical procedures, holds promise as a valuable tool, alongside the historically established BDL model.

One notable feature of this model is the increased fibrinolysis (Fig. 6). In the pathophysiology associated with fibrinolysis during liver dysfunction, fibrin deposition is a recognized phenomenon in various liver injury models, with diverse characteristics in deposition sites (37–40). Notably, fibrin deposition in acute cholestatic liver injury induced by complete bile duct obstruction or single-dose ANIT administration to mice produces a distinctive histological pattern, extensively researched by Luyendyk's group (41–43). This group reports that ANIT-like fibrin deposition is observed in patients with primary biliary cholangitis (PBC) and primary sclerosing cholangitis (PSC). Models exhibiting ANIT-like fibrin deposition would contribute to understanding the pathophysiology of these diseases (43). Considering the hepatotoxicity to bile ducts induced by MDA, it is inferred that the MDA-DW model also presents the pathophysiology of ANIT-like fibrin deposition. Indeed, distinctive structures are observed through H&E staining at day 7 and 14 of administration (Fig 1, 2). As ANIT has low solubility and the preparation of ANIT-containing diets is costly for longitudinal analysis, the proposed model could be a useful tool to deepen our understanding of the characteristic fibrin deposition in liver dysfunction, although further investigation is required for fibrin deposition in the MDA-DW model.

A unique contribution of this study, not underscored in the preceding discussions, is the acquisition of biochemical test values, transcriptome profiles, and immune cell trafficking data from identical subjects at five time points for both the MDA-DW and TAA-DW models (Fig 2). We believe this multi-view data is valuable resources contributing to the understanding of the temporal changes during liver injury, particularly the relationship between the molecular biology state of the liver and the behavior of immune cells. The accumulation of such longitudinal and comparable data would create a foundation for comprehensive analyses, fostering insights into the pathophysiological mechanisms underlying the progression of liver dysfunction.

Acknowledgements

We thank all those who contributed to the construction of the data sets employed in the present study such as CEBS, Open TG-GATEs, and DrugMatrix. We also thank Dr. Toru Komatsu (the University of Tokyo) for funding and helpful discussion.

Abbreviations

MDA, 4,4'-methylenedianiline; TAA, thioacetamide; ALT, alanine aminotransferase; AST, aspartate aminotransferase; GO, Gene Ontology; GAGE, Generally Applicable Gene-set Enrichment; ANIT, α-naphthylisothiocyanate; HSCs, hepatic stellate cells; PFs, portal fibroblasts

References

1. Balakrishnan M, Rehm J. A public health perspective on mitigating the global burden of chronic liver disease. Hepatology. 2024;79:451–459.
2. Ibrahim SH, Kamath BM, Loomes KM, Karpen SJ. Cholestatic liver diseases of genetic etiology: Advances and controversies. Hepatology. 2022;75:1627–1646.
3. Tsuchida T, Lee YA, Fujiwara N, Ybanez M, Allen B, Martins S, et al. A simple diet- and chemical-induced murine NASH model with rapid progression of steatohepatitis, fibrosis and liver cancer. J Hepatol. 2018;69:385–395.
4. Scholten D, Trebicka J, Liedtke C, Weiskirchen R. The carbon tetrachloride model in mice. Lab Anim. 2015;49:4–11.
5. Jaeschke H, Williams CD, Ramachandran A, Bajt ML. Acetaminophen hepatotoxicity and repair: the role of sterile inflammation and innate immunity. Liver Int. 2012;32:8–20.
6. Tanaka Y, Aleksunes LM, Cui YJ, Klaassen CD. ANIT-Induced Intrahepatic Cholestasis Alters Hepatobiliary Transporter Expression via Nrf2-Dependent and Independent Signaling. Toxicological Sciences. 2009;108:247–257.
7. Yang X, Greenhaw J, Shi Q, Roberts DW, Hinson JA, Muskhelishvili L, et al. Mouse Liver Protein Sulfhydryl Depletion after Acetaminophen Exposure. Journal of Pharmacology and Experimental Therapeutics. 2013;344:286–294.
8. Heymann F, Hamesch K, Weiskirchen R, Tacke F. The concanavalin A model of acute hepatitis in mice. Lab Anim. 2015;49:12–20.
9. Nakama T. Etoposide prevents apoptosis in mouse liver with ?-galactosamine/lipopolysaccharide-induced fulminant hepatic failure resulting in reduction of lethality. Hepatology. 2001;33:1441–1450.
10. Kwon S-B, Park J-S, Yi J-Y, Hwang J-W, Kim M, Lee M-O, et al. Time- and Dose-based Gene Expression Profiles Produced by a Bile-duct–damaging Chemical, 4,4′-methylene Dianiline, in Mouse Liver in an Acute Phase. Toxicol Pathol. 2008;36:660–673.
11. Scholten D, Trebicka J, Liedtke C, Weiskirchen R. The carbon tetrachloride model in mice. Lab Anim. 2015;49:4–11.
12. Wang X, Lopategi A, Ge X, Lu Y, Kitamura N, Urtasun R, et al. Osteopontin induces ductular reaction contributing to liver fibrosis. Gut. 2014;63:1805–18.
13. Salguero Palacios R, Roderfeld M, Hemmann S, Rath T, Atanasova S, Tschuschner A, et al. Activation of hepatic stellate cells is associated with cytokine expression in thioacetamide-induced hepatic fibrosis in mice. Lab Invest. 2008;88:1192–203.
14. Kwon S-B, Park J-S, Yi J-Y, Hwang J-W, Kim M, Lee M-O, et al. Time- and dose-based gene expression profiles produced by a bile-duct-damaging chemical, 4,4'-methylene dianiline, in mouse liver in an acute phase. Toxicol Pathol. 2008;36:660–73.
15. Lamb JC, Huff JE, Haseman JK, Murthy AS, Lilja H. Carcinogenesis studies of 4,4'-methylenedianiline dihydrochloride given in drinking water to F344/N rats and B6C3F1 mice. J Toxicol Environ Health. 1986;18:325–37.
16. Waters M, Stasiewicz S, Merrick BA, Tomer K, Bushel P, Paules R, et al. CEBS--Chemical Effects in Biological Systems: a public data repository integrating study design and toxicity data with microarray and proteomics data. Nucleic Acids Res. 2008;36:D892-900.
17. Igarashi Y, Nakatsu N, Yamashita T, Ono A, Ohno Y, Urushidani T, et al. Open TG-GATEs: a large-scale toxicogenomics database. Nucleic Acids Res. 2015;43:D921-7.
18. Ganter B, Snyder RD, Halbert DN, Lee MD. Toxicogenomics in drug discovery and development: mechanistic analysis of compound/class-dependent effects using the DrugMatrix database. Pharmacogenomics. 2006;7:1025–44.
19. Ma R, Sun ED, Zou J. A spectral method for assessing and combining multiple data visualizations. Nat Commun. 2023;14:780.
20. Liberzon A, Subramanian A, Pinchback R, Thorvaldsdóttir H, Tamayo P, Mesirov JP. Molecular signatures database (MSigDB) 3.0. Bioinformatics. 2011;27:1739–40.
21. Luo W, Friedman MS, Shedden K, Hankenson KD, Woolf PJ. GAGE: generally applicable gene set enrichment for pathway analysis. BMC Bioinformatics. 2009;10:161.

22. Eisinga R, Breitling R, Heskes T. The exact probability distribution of the rank product statistics for replicated experiments. FEBS Lett. 2013;587:677–682.
23. Kopelman H, Robertson MH, Sanders PG, Ash I. The Epping jaundice. Br Med J. 1966;1:514–6.
24. Hossain M, Kubes P. Innate immune cells orchestrate the repair of sterile injury in the liver and beyond. Eur J Immunol. 2019;49:831–841.
25. Yang R, Tonnesseen TI. DAMPs and sterile inflammation in drug hepatotoxicity. Hepatol Int. 2019;13:42–50.
26. Liu K, Wang F-S, Xu R. Neutrophils in liver diseases: pathogenesis and therapeutic targets. Cell Mol Immunol. 2021;18:38–44.
27. Saijou E, Enomoto Y, Matsuda M, Yuet-Yin Kok C, Akira S, Tanaka M, et al. Neutrophils alleviate fibrosis in the CCl4-induced mouse chronic liver injury model. Hepatol Commun. 2018;2:703–717.
28. Hatada S, Ohta T, Shiratsuchi Y, Hatano M, Kobayashi Y. A novel accessory role of neutrophils in concanavalin A-induced hepatitis. Cell Immunol. 2005;233:23–29.
29. Beattie L, Sawtell A, Mann J, Frame TCM, Teal B, de Labastida Rivera F, et al. Bone marrow-derived and resident liver macrophages display unique transcriptomic signatures but similar biological functions. J Hepatol. 2016;65:758–768.
30. Lamb J, Crawford ED, Peck D, Modell JW, Blat IC, Wrobel MJ, et al. The Connectivity Map: using gene-expression signatures to connect small molecules, genes, and disease. Science. 2006;313:1929–35.
31. Nemoto S, Morita K, Mizuno T, Kusuhara H. Decomposition Profile Data Analysis for Deep Understanding of Multiple Effects of Natural Products. J Nat Prod. 2021;84:1283–1293.
32. Morita K, Mizuno T, Kusuhara H. Decomposition profile data analysis of multiple drug effects identifies endoplasmic reticulum stress-inducing ability as an unrecognized factor. Sci Rep. 2020;10:13139.
33. Nikolaev V, Kerimova M, Naydenova E, Ivanov E, Adjarov D. Biochemical changes in the rat after chronic thioacetamide intoxication. Toxicology. 1988;48:81–5.
34. Wallace M, Hamesch K, Lunova M, Kim Y, Weiskirchen R, Strnad P, et al. Standard Operating Procedures in Experimental Liver Research: Thioacetamide model in mice and rats. Lab Anim. 2015;49:21–29.
35. Iwaisako K, Brenner DA, Kisseleva T. What's new in liver fibrosis? The origin of myofibroblasts in liver fibrosis. J Gastroenterol Hepatol. 2012;27 Suppl 2:65–8.
36. Iwaisako K, Jiang C, Zhang M, Cong M, Moore-Morris TJ, Park TJ, et al. Origin of myofibroblasts in the fibrotic liver in mice. Proc Natl Acad Sci U S A. 2014;111:E3297-305.
37. Whipple GH, Hurwitz SH. FIBRINOGEN OF THE BLOOD AS INFLUENCED BY THE LIVER NECROSIS OF CHLOROFORM POISONING. J Exp Med. 1911;13:136–61.
38. Neubauer K, Knittel T, Armbrust T, Ramadori G. Accumulation and cellular localization of fibrinogen/fibrin during short-term and long-term rat liver injury. Gastroenterology. 1995;108:1124–35.
39. Hewett JA, Roth RA. The coagulation system, but not circulating fibrinogen, contributes to liver injury in rats exposed to lipopolysaccharide from gram-negative bacteria. J Pharmacol Exp Ther. 1995;272:53–62.
40. Okajima K, Harada N, Kushimoto S, Uchiba M. Role of microthrombus formation in the development of ischemia/reperfusion-induced liver injury in rats. Thromb Haemost. 2002;88:473–80.
41. Kopec AK, Luyendyk JP. Role of Fibrin(ogen) in Progression of Liver Disease: Guilt by Association? Semin Thromb Hemost. 2016;42:397–407.
42. Luyendyk JP, Cantor GH, Kirchhofer D, Mackman N, Copple BL, Wang R. Tissue factor-dependent coagulation contributes to alpha-naphthylisothiocyanate-induced cholestatic liver injury in mice. Am J Physiol Gastrointest Liver Physiol. 2009;296:G840-9.
43. Luyendyk JP, Kassel KM, Allen K, Guo GL, Li G, Cantor GH, et al. Fibrinogen deficiency increases liver injury and early growth response-1 (Egr-1) expression in a model of chronic xenobiotic-induced cholestasis. Am J Pathol. 2011;178:1117–25.

Tables

We thank all those who contributed to the construction of the data sets employed in the present study such as CEBS, Open TG-GATEs, and DrugMatrix. We also thank Dr. Toru Komatsu (the University of Tokyo) for funding and helpful discussion.

Figure legends

Figure 1. Induction of liver injury via the oral administration of MDA in drinking water.
(a) Time course of changes in ALT. (b) Quantitative PCR evaluations of fibrosis markers at each time interval. Error bars represent standard deviation. HE stained images of liver tissue (day7) from control (c), TAA (d), and MDA (e) groups.

Figure 2. The detection of abnormal regions in pathological images.
(a) Visualization of PCA of feature vectors for each patch and results of anomaly detection (day7). 1 indicates normal patches; -1 indicates anomalous patches. (b, c) Visualization of anomalous patches on the images. No.13, TAA (day7); No.27, MDA (day7). (d, e) Original H&E stained images. (f) Visualization of each anomalous patch. Numbers correspond to those in a, b, c.

Figure 3. Experimental design of multi-view data acquisition
Blood and liver samples are obtained from each individual to provide multi-view data linking the compound administered, time post-administration, blood biochemistry values, immune cell trafficking, and transcriptome data.

Figure 4. Comparison of changes in blood biochemistry values between MDA-DW and TAA-DW models
The figure illustrates the time course of changes in blood biochemistry values: (a) ALT and AST, (b) TBIL, and (c) TCHO. Error bars are indicative of standard deviation. It should be noted that the scale on the x-axis does not correspond to actual time. ALT, alanine aminotransferase; AST, aspartate aminotransferase; TBIL, total bilirubin; TCHO, total cholesterol Alterations in markers of liver injury during the early phase of models.

Figure 5. Comparison of immune cell trafficking between MDA-DW and TAA-DW models
(a)The violin plots represent the variation in immune cell proportion at different time points. It should be noted that the scale on the x-axis does not correspond to actual time. MonMac, monocyte-derived macrophages. (b)Visualization of the correlation between ALT and Neutrophil levels. The filled color surrounding the line indicates the 95% confidence interval.

Figure 6. Comparison of transcriptome profiles between MDA-DW and TAA-DW models
Transcriptome profiles were embedded in 2-dimensions with meta-visualization, a dimension-reduction method (19). The embedded values were plotted for visualizing two aspects: (a) temporal changes and (b) associations with ALT values.

Figure 7. Gene set analysis of MDA-DW and TAA-DW models
Characteristic Gene Ontology (GO) terms of MDA-DW and TAA-DW models are visualized. (a) The vertical axis represents the GAGE mean difference, and the horizontal axis represents time. The circle size at each point corresponds to the -log(p) value calculated by GAGE.

Figures

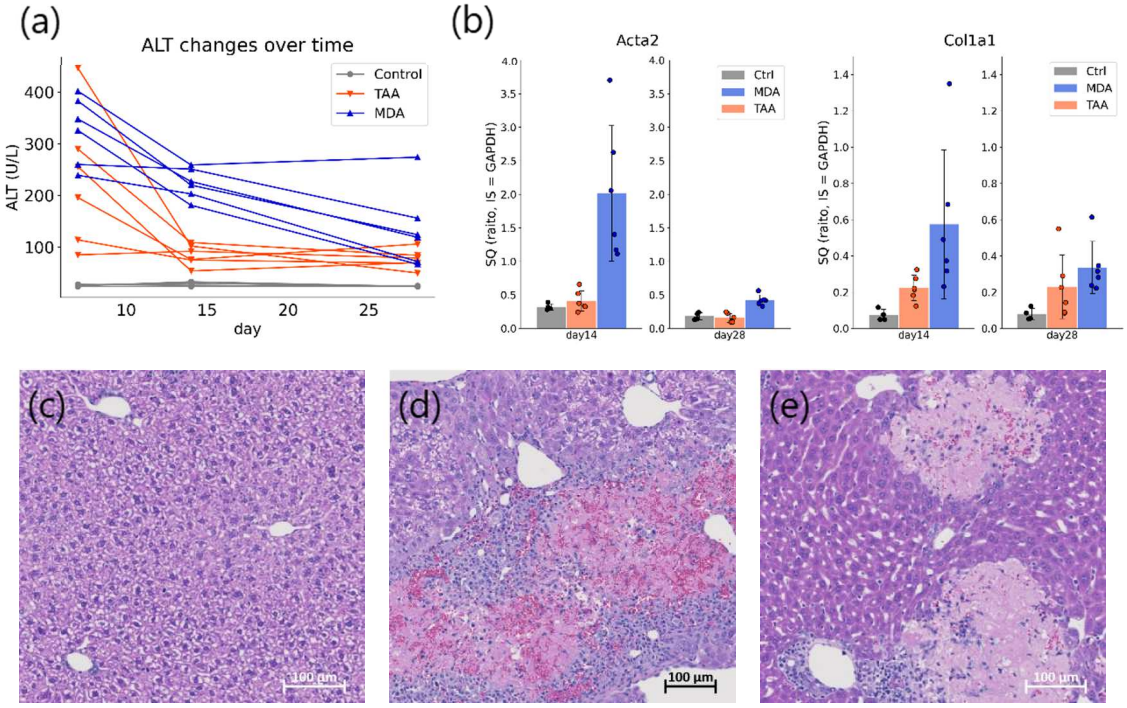

Figure 1.

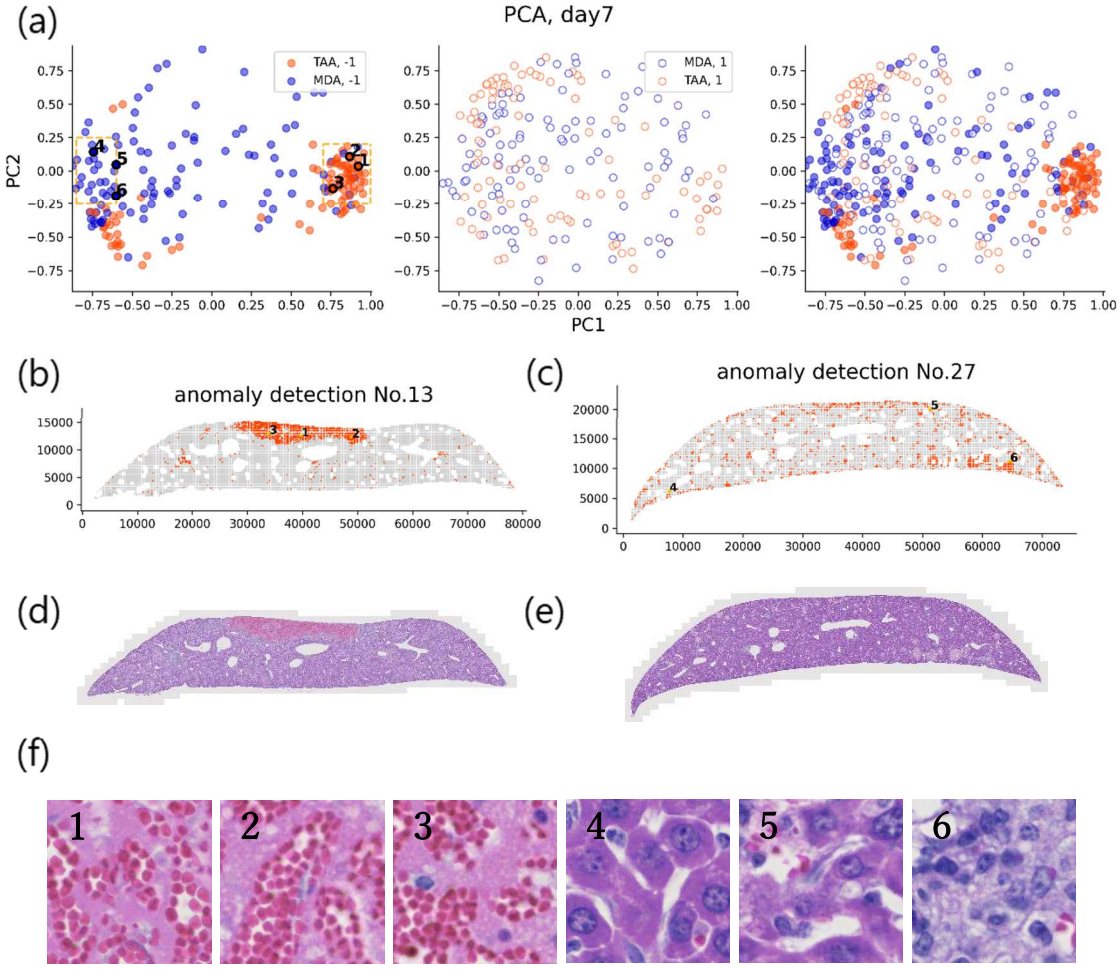
(a)
PCA, day7
TAA, -1
MDA, -1
MDA, 1
TAA, 1
PC2
PC1
(b)
anomaly detection No.13
(c)
anomaly detection No.27
(d)
(e)
(f)
1
2
3
4
5
6

Figure 2.

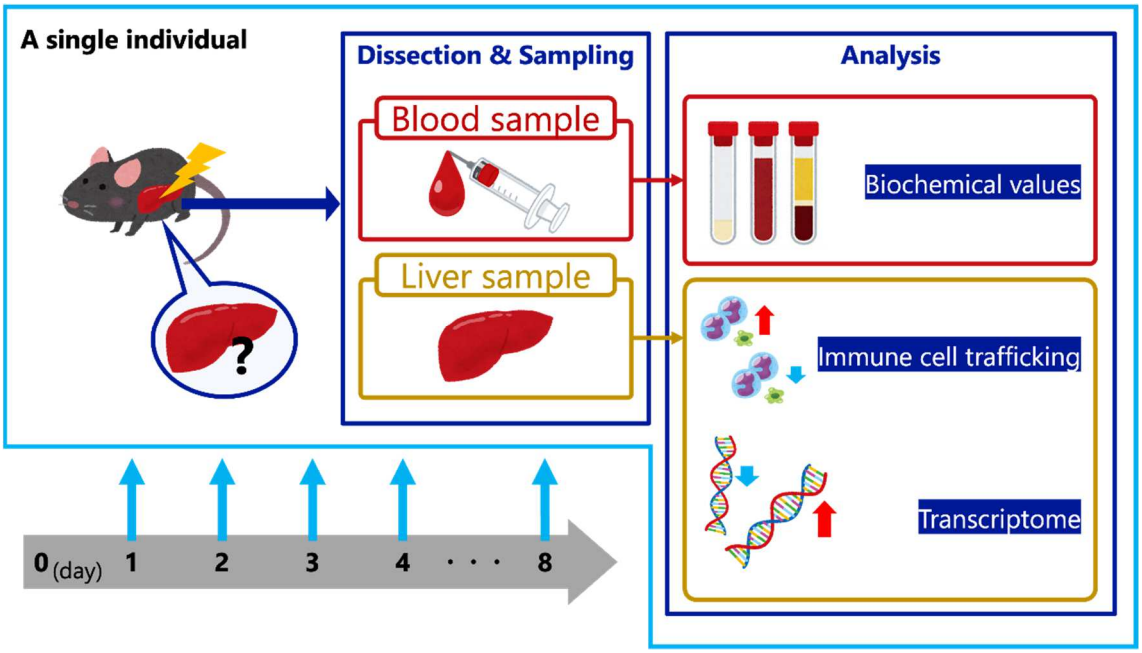
A single individual
Dissection & Sampling
Blood sample
Liver sample
Analysis
Biochemical values
Immune cell trafficking
Transcriptome
0 (day)
1
2
3
4
8

Figure 3.

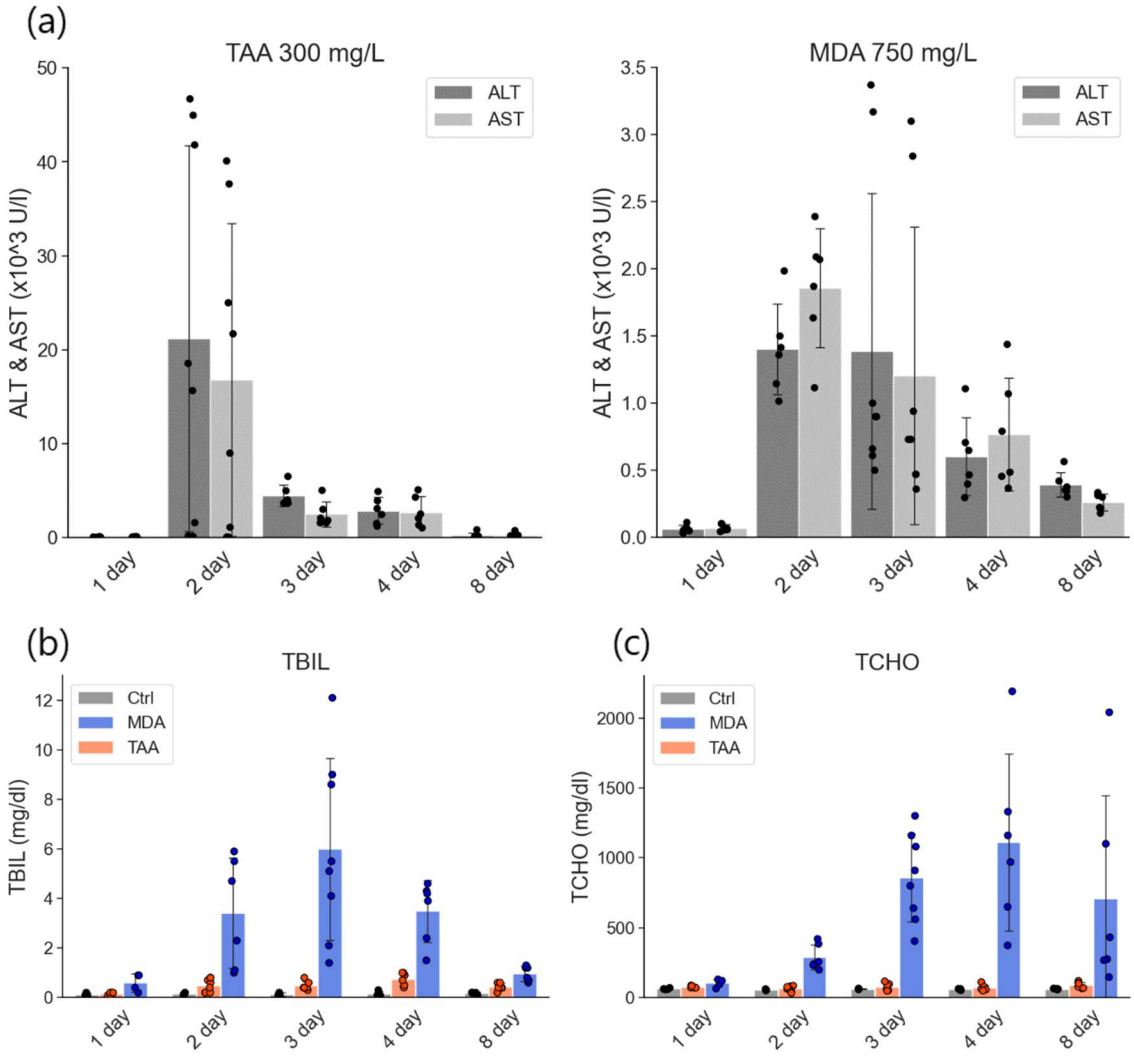
(a)
TAA 300 mg/L
MDA 750 mg/L
ALT
AST
ALT & AST (x10^3 U/l)
1 day
2 day
3 day
4 day
8 day
(b)
TBIL
Ctrl
MDA
TAA
TBIL (mg/dl)
(c)
TCHO
TCHO (mg/dl)

Figure 4.

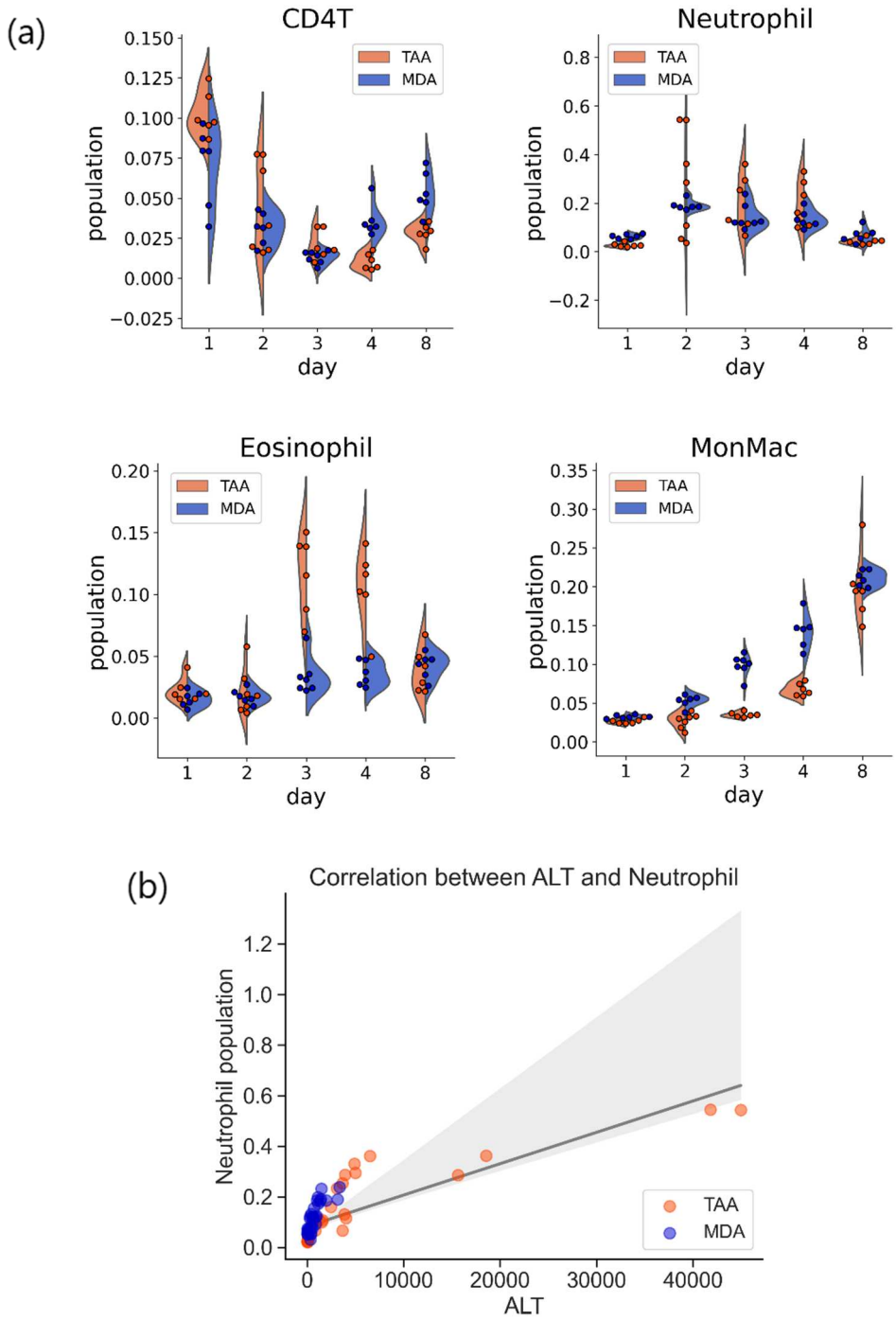
(a)
CD4T
Neutrophil
Eosinophil
MonMac
TAA
MDA
population
day
(b)
Correlation between ALT and Neutrophil
Neutrophil population
ALT
TAA
MDA

Figure 5.

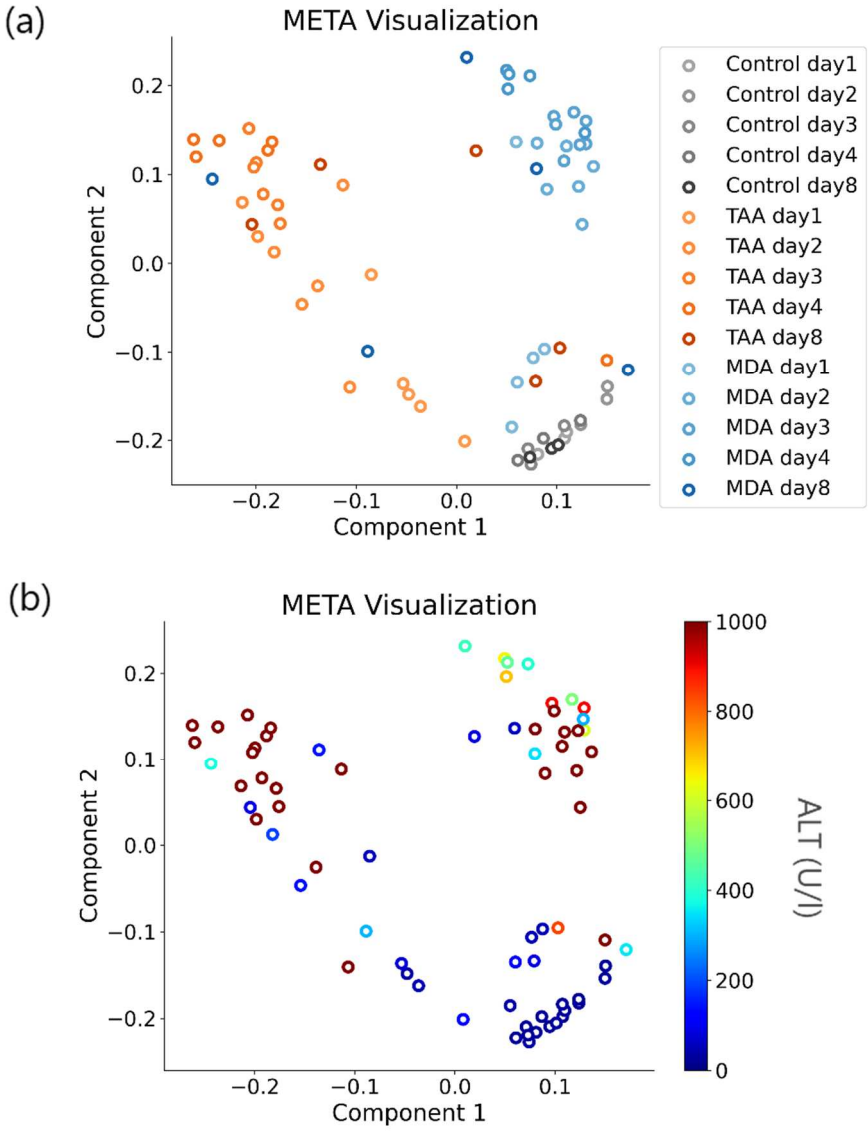
(a)
META Visualization
Component 2
Component 1
0.2
0.1
0.0
−0.1
−0.2
Control day1
Control day2
Control day3
Control day4
Control day8
TAA day1
TAA day2
TAA day3
TAA day4
TAA day8
MDA day1
MDA day2
MDA day3
MDA day4
MDA day8
(b)
META Visualization
ALT (U/l)
1000
800
600
400
200
0

Figure 6.

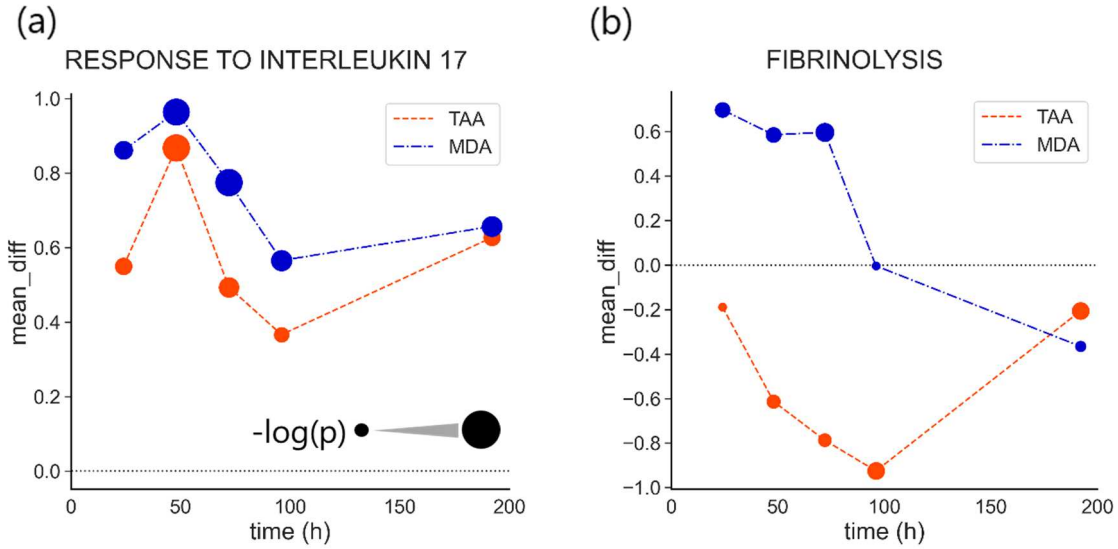
(a)
RESPONSE TO INTERLEUKIN 17
TAA
MDA
mean_diff
time (h)
-log(p)
(b)
FIBRINOLYSIS
TAA
MDA
mean_diff
time (h)

Figure 7.

Supplementary Information for "Establishment of an easy-to-construct liver injury mouse model for longitudinal analysis by drinking-water administration of MDA"

Takumi Iwasaka[1, *], Tadahaya Mizuno[2, *, †], Katsuhisa Morita[1], Iori Azuma[1], Tomoka Nakagawa[1], Eri Nakashima[1], Hiroyuki Kusuhara[1]

[1]Graduate School of Pharmaceutical Sciences, the University of Tokyo, Bunkyo-ku, Tokyo, 113-0033, Japan
[2]Graduate School of Pharmaceutical Sciences, the University of Tokyo, Bunkyo-ku, Tokyo, 113-0033, Japan, Electronic address: tadahaya@gmail.com
†Corresponding author: Tadahaya Mizuno
*These authors contributed equally.

Supplementary Methods

RNA-seq analysis

Poly(A) tailed mRNA was purified from total RNA prepared with Isogen II (311-07361, Nippon Gene, Japan) using the NEBNext Poly(A) mRNA Magnetic Isolation Module. RNA-Seq libraries were prepared using the NEBNext Ultra II Directional RNA Library Prep Kit for Illumina. Libraries were sequenced using the NovaSeq 6000 S1 Rgt Kit v1.5 (200 cyc).

Quality control of all reads was performed using PRINSEQ++ (version 1.2.4) with the indicated parameters (trim_left=5, trim_tail_right=5, trim_qual_right=30, ns_max_n=20, min_len=30) (https://peerj.com/preprints/27553/). The Expression of transcripts was quantified using Salmon (version 1.6.0) and gencode.vM28.transcripts obtained from GENCODE (https://www.gencodegenes.org/) with the indicated parameters (validationMappings, gcBias, seqBias) and decoy-aware index created using Salmon and GRCm39.primary_assembly.genome obtained from GENCODE (1). Transcripts Per Kilobase Million (TPM) data was obtained using tximport which is implemented in the software package Bioconductor with R (version 4.2.3) from quant.sh files created by Salmon (version 1.8.0)(2).

Flow cytometry analysis

The liver sample was dissociated using gentleMACS according to the manufacturer's instructions. Except noted especially, PBS containing 2% fetal bovine serum was used as "Wash Buffer" thereafter. The washed samples were centrifuged (50×g, 4 °C for 3 min) to eliminate hepatocytes and were subjected to ACK Lysis Buffer. ACK buffer was prepared by adding 8,024 mg of NH4Cl (A2037, TCI, Japan), 10 mg of NHCO3 (166-03275, FUJIFILM Wako, Japan), and 3.772 mg of EDTA 2Na · 2H2O (6381-92-6, Dojindo Laboratories, Japan) into 1 L pure water. The samples were washed with the Wash Buffer three times and then the samples were subjected to flow cytometry analysis. Flow cytometric analysis was performed with FACSCelesta (BD Biosciences, USA), and data were analyzed with FlowJo software (Treestar). Proportions of NK cells (CD45+/CD3−/NK1.1+), B cells (CD45+/B220+), CD4+ T cells (CD45+/CD3+/B220−/CD4+), CD8+ T cells (CD45+/CD3+/B220−/CD4−/CD8a+), NKT cells (CD45+/CD3+/B220−/CD4−/CD8a−/NK1.1+), γδT cells (CD45+/CD3+/B220−/CD4−/CD8a−/gdTCR+), eosinophils (CD45+/CD11b+/Siglec-F+), neutrophils (CD45+/CD11b+/Siglec-F−/Ly6G+/Tim4−), monocytes (CD45+/CD11b+/Siglec-F−/Ly6G−/Tim4−/Ly6C+), monocyte-derived macrophages

(CD45+/CD11b+/Siglec-F−/Ly6G−/Tim4−/Ly6C−), and Kupffer cells (CD45+/CD11b+/Siglec-F−/Ly6G−/Tim4+/Ly6C−) were acquired via flow cytometry. The antibodies used are listed in Supplementary Table S6.

Histopathological analysis with a deep learning model

The deep learning framework PyTorch version 2.0.1 was employed for this study. Deep learning and feature extraction tasks were carried out utilizing the FUJITSU Supercomputer PRIMEHPC FX1000 and FUJITSU Server PRIMERGY GX2570 (Wisteria/BDEC-01) at the Information Technology Center, The University of Tokyo. Python (version 3.11.3) with open-source packages was utilized for all analyses except for deep learning.

Pathological images of the liver were collected from the Open TG-GATEs (TGGATEs) database, along with corresponding pathological finding type annotations and individual rat information from TogoDB. These images were acquired at 20× magnification using Aperio ScanScope AT. The dataset preparation involved excluding compounds not sampled at all specified time points and limiting samples to the highest compound concentration. Subsequently, one control sample per condition and one image per individual were randomly selected, resulting in a dataset of 6508 whole slide images (WSI) for the liver. The construction of the finding-based model followed our previous work on expression learning based on pathological findings (3), with some differences such as varying image sizes and multi-label learning. The Open TG-GATEs dataset was split into Train1 and Test subsets in a 4:1 ratio, further split into Train2 and Validation subsets in a 4:1 ratio. Weak labels were generated through multi-label training using patches of pathological images and corresponding labels from the Train2 subset, focusing on eight pathological findings: proliferation bile duct, ground glass appearance, increased mitosis, inclusion body intracytoplasmic, deposit pigment, single cell necrosis, vacuolization cytoplasmic, and swelling. The model predicted the probability of these findings in images of the validation subset, repeated five times to apply resulting labels to Train1 subset patches. Patches were extracted based on predicted probabilities, and a new model was trained using these patches and corresponding probabilities for training of the finding-based model.

The formalin-fixed liver specimens underwent standard processing procedures, including slicing into 4 μm sections, staining with hematoxylin and eosin (H&E), and visualization using ZEISS Axio Scan.Z1.

Subsequently, the whole slide images (WSI) were partitioned into patches of 256×256 pixels, and feature extraction was performed on each patch using the aforementioned model. After extracting features from the fourth layer, one class support vector machine (sklearn, version 1.4.1) was employed to classify whether each patch was anomalous or not. Additionally, dimensionality reduction of the features was achieved through PCA and visualized. Details are available on our GitHub repository (https://github.com/mizuno-group/MDAdrinkingwater).

Supplementary Figures and Tables

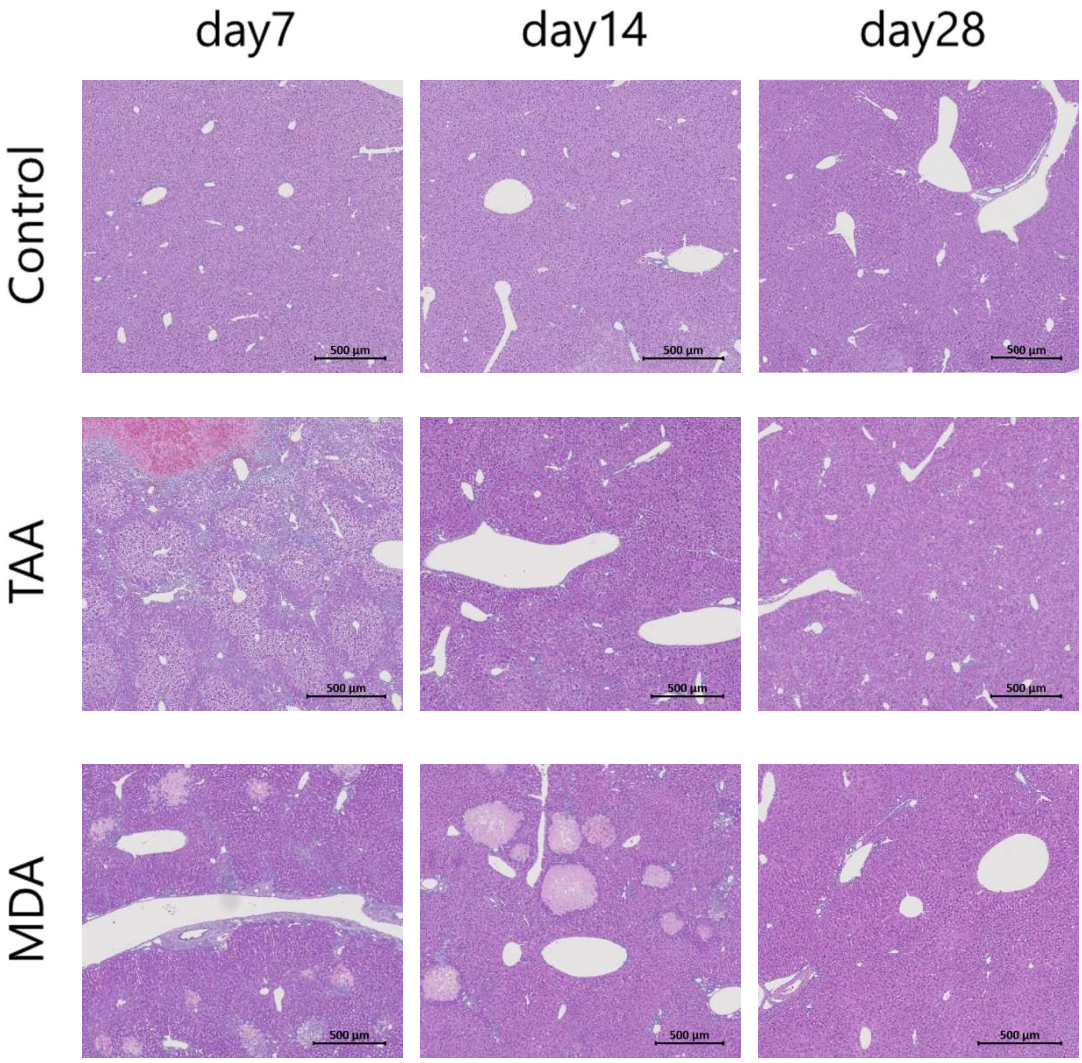

Figure S1. The figure displays HE stained in livers.
HE stained images of liver tissue (day7, 14, 28) from control, TAA (300 mg/l), and MDA (750 mg/l) groups.

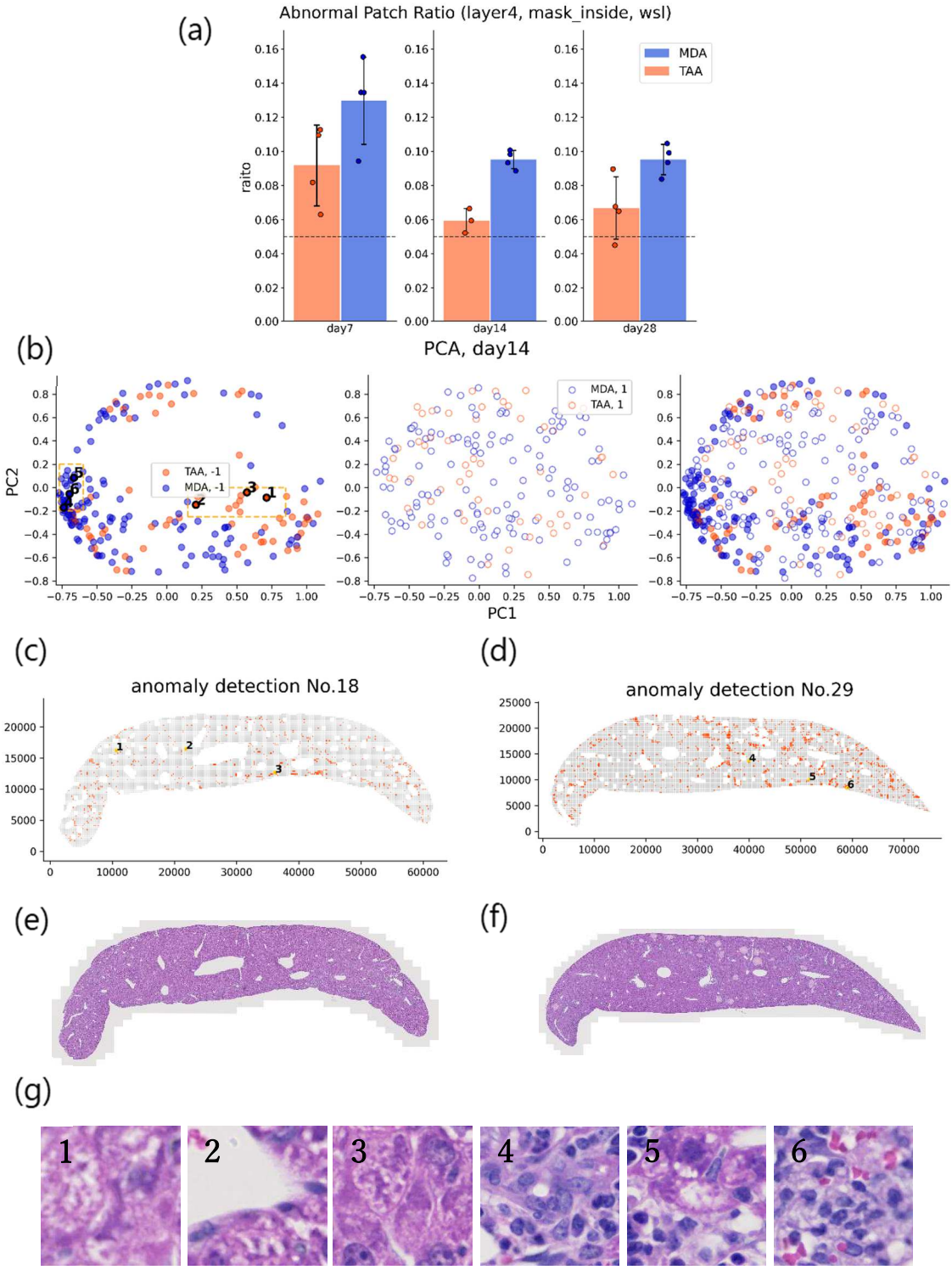

Figure S2. The detection of abnormal regions in pathological images.
(a) The proportion of anomalous patches at each time point. Dotted lines represent the value of nu in the one-class SVM. (b) Visualization of PCA of feature vectors for each patch and results of anomaly detection (day14). 1 indicates normal patches; -1 indicates anomalous patches. (c, d) Visualization of anomalous patches on the images. No.18, TAA (day14); No.29, MDA (day14). (e, f) Original H&E stained images. (g) Visualization of each anomalous patch. Numbers correspond to those in b, c, d.

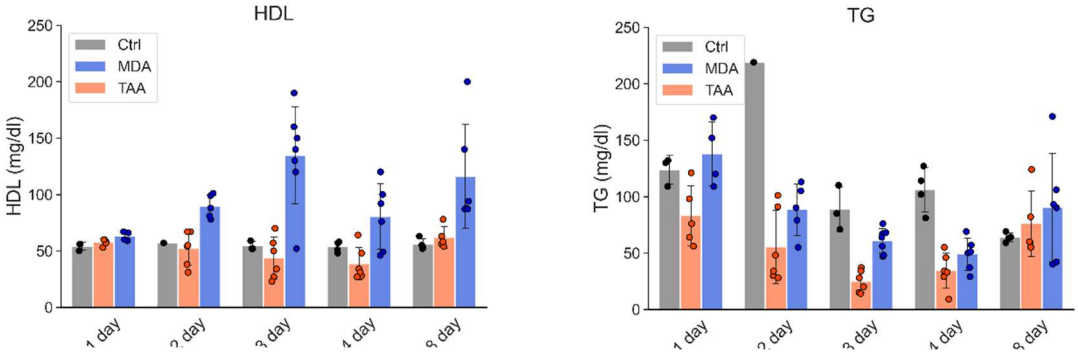

Figure S3. Comparison of changes in blood biochemistry values between MDA-DW and TAA-DW models.

The figure illustrates the time course of changes in blood biochemistry values. Error bars are indicative of standard deviation. It should be noted that the scale on the x-axis does not correspond to actual time. HDL, High Density Lipoprotein; TG, triglyceride.

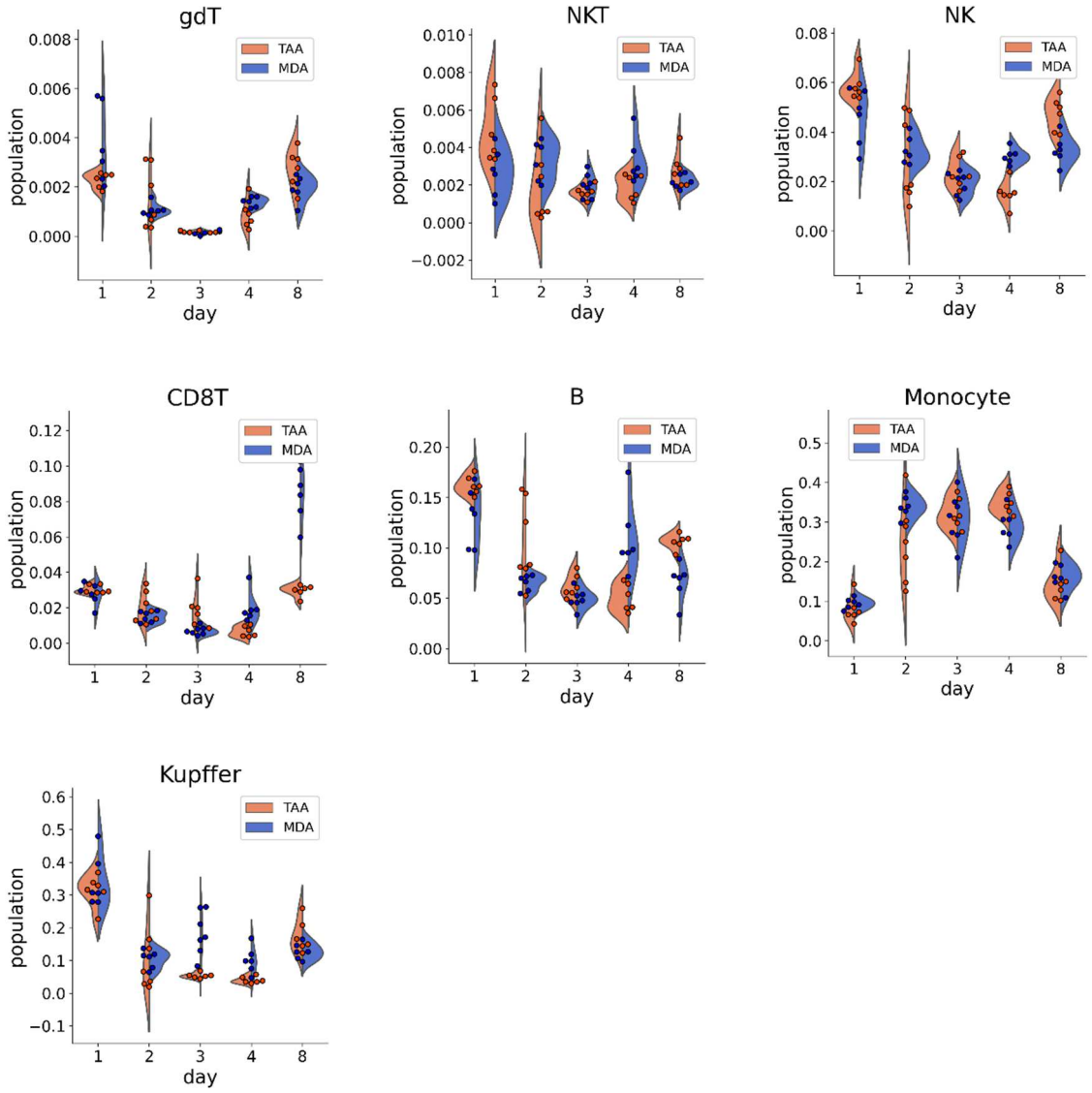

Figure S4. Violin plot for immune cell populations after administration.
The violin plots represent the variation in immune cell proportion at different time points. It should be noted that the scale on the x-axis does not correspond to actual time.

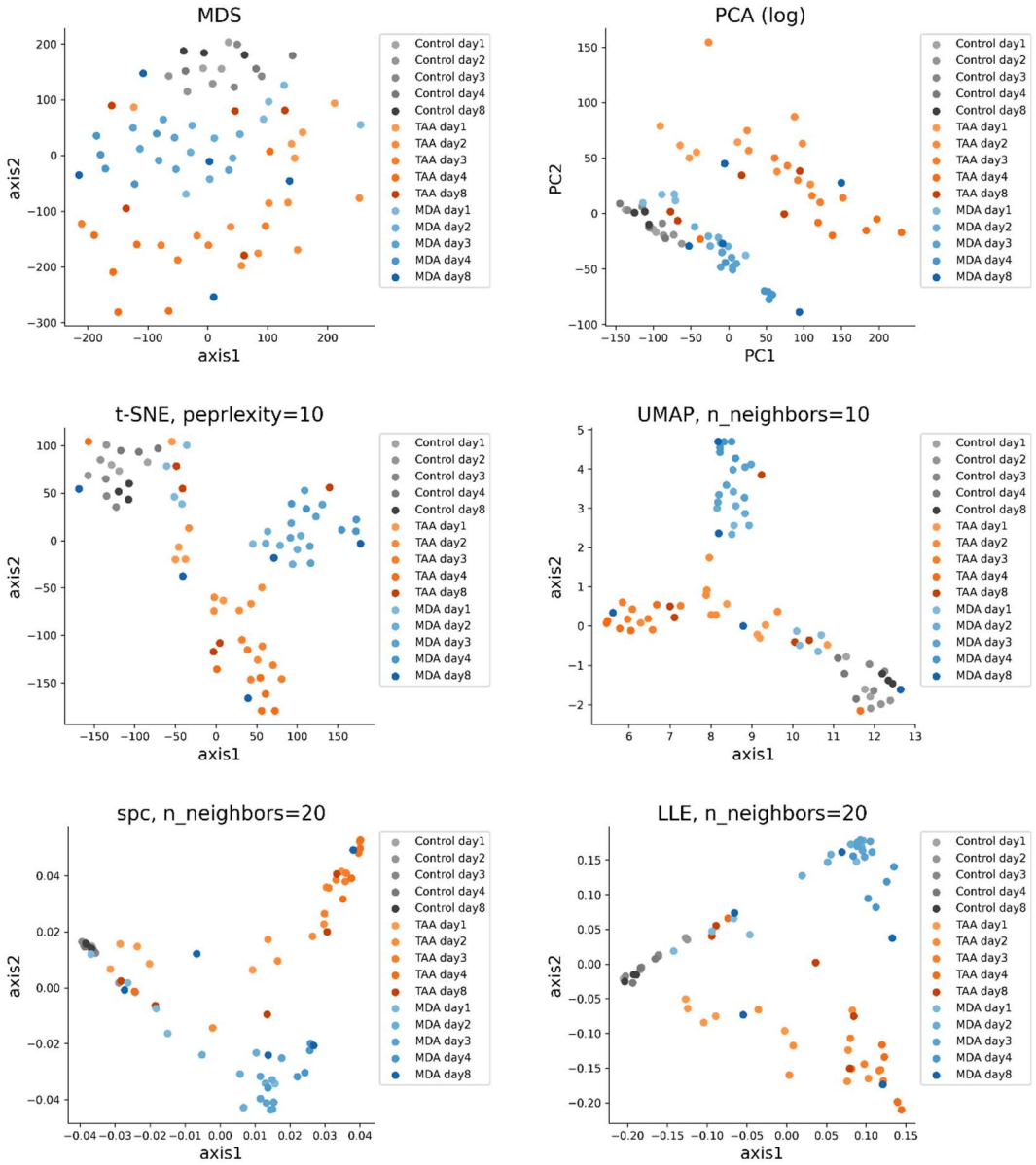

Figure S4. Visualization of transcriptome data embedded in 2D with each method constituting meta-visualization.

The numerical value provided alongside the title represents the specified hyperparameter value. PCA, principal component analysis; MDS, multidimensional scaling; t-SNE, t distributed stochastic neighbor embedding; UMAP, uniform manifold approximation and projection; spc, spectral embedding; LLE, locally linear embedding.

References

1. Frankish A, Diekhans M, Ferreira A-M, Johnson R, Jungreis I, Loveland J, et al. GENCODE reference annotation for the human and mouse genomes. Nucleic Acids Res. 2019;47:D766–D773.
2. Patro R, Duggal G, Love MI, Irizarry RA, Kingsford C. Salmon provides fast and bias-aware quantification of transcript expression. Nat Methods. 2017;14:417–419.
3. Maedera S, Mizuno T, Kusuhara H. Investigation of latent representation of toxicopathological images extracted by CNN model for understanding compound properties in vivo. Comput Biol Med. 2024;168:107748.